EPJ Web of Conferences **346**, 02009 (2026) https://doi.org/10.1051/epjconf/202634602009
RFPPC2025

ICRF near-field effects sensitivity to magnetic tilt-angle

Guillaume Urbanczyk[a,b*], *Syun'ichi* Shiraiwa[c], *Nicola* Bertelli[c], *Wouter* Tierens[d], *Roberto* Bilato[b], *Volodymyr* Bobkov[b], *Roman* Ochoukov[b], *Ralph* Dux[b], *Laurent* Colas[e], *James-Paul* Gunn[e], *Julien* Hillairet[e], *Nicolas* Fedorczak[e], *Raymond* Diab[f], *Léonel Tsowémoo* Faabomvé[a], *Jérôme* Moritz[a], *Stéphane* Heuraux[b], ASDEX Upgrade Team[+], WEST Team, and EUROfusion Tokamak Exploitation Team[++]

[a] Institut Jean Lamour UMR 7198 CNRS - Université de Lorraine 2 allée André Guinier F-54011 Nancy, France
[b] Max-Planck-Institut für Plasmaphysik, Boltzmannstrasse 2, D-85748 Garching, Germany
[c] Princeton Plasma Physics Laboratory, Princeton, NJ 08540, United States of America
[d] Oak Ridge National Laboratory, Oak Ridge, TN, United States of America
[e] CEA, IRFM, F-13108 Saint Paul-Lez-Durance, France
[f] Plasma Science and Fusion, Massachusetts Institute of Technology, Cambridge, MA, USA

+ See author list of H. Zohm et al 2024 Nucl. Fusion 64 112001
++ See the author list of E. Joffrin et al 2024 Nucl. Fusion 64 112019

Abstract. This paper complements the study reported in *G. Urbanczyk et al 2025 Nucl. Fusion 65 046018* by investigating how near-field effects from Ion Cyclotron Range of Frequency (ICRF) antennas depend on the magnetic geometry, particularly focusing on the sensitivity of rectified sheath potentials and associated impurity production to variations in magnetic field tilt-angle. Simulations were conducted using Petra-M, employing a flat model of the ASDEX Upgrade (AUG) three-strap antenna, and COMSOL, utilizing a curved model of the WEST antenna. Results demonstrate indications of sensitivity of the rectified sheath potentials and impurity sputtering to the alignment of Faraday screen bars with the magnetic field lines, emphasizing the necessity for careful consideration of geometric alignment in antenna design for fusion devices. This trend is consistent with experimental data measured with various diagnostics.

1 Introduction

Understanding Ion Cyclotron Range of Frequency (ICRF)-induced sheath potentials and associated impurity sputtering is critical for the efficient and safe operation of fusion reactors. Near-field effects, induced at ICRF antenna limiters, locally enhance plasma-material interactions, potentially leading to increased impurity production and reduced component lifetimes. Investigating the sensitivity of these near-field effects to variations in magnetic geometry, specifically the magnetic field tilt-angle, is thus essential.

Experimentally – assuming all physical parameters are uniform along a given magnetic field line – this sensitivity is often studied by constructing radial-poloidal 2D maps of various parameters such as

- plasma potential with reciprocating emissive probe in WEST [1]
- ion energy with Retarded Field Analyzer in Tore Supra [2] and ASDEX Upgrade (AUG) [3]
- density in JET [4, 5].

For each plasma current (or q_{95}), radial profiles are measured by different diagnostics positioned at some distance from the powered ICRF antenna. These diagnostics magnetically connect to different poloidal locations on the antenna limiter depending on the plasma current. This methodology has been widely applied across several tokamaks, often revealing potential peaks at antenna corners.

However, interpreting these constructed 2D maps as instantaneous snapshots relies on three crucial assumptions: (1) the measured parameter remains insensitive to changes in plasma current (and hence magnetic field tilt-angle), (2) RF sheath effects remain insensitive to plasma current variations, and (3) observed variations predominantly result from local RF sheath-induced effects. When looking at tungsten (W) gross erosion along AUG antenna limiter with visible spectroscopy (cf. Figure 1), amplitude and location of maxima change substantially during the plasma current scan, revealing hidden dependencies that are somewhat assumed negligible for the analysis.

With our main motivations emerging from previous analysis of AUG experiments reported in [3], we now evaluate the validity of these implicit assumptions through comparative numerical simulations using Petra-M and COMSOL codes. Simulations maintain constant coupled power, while systematically varying the magnetic field tilt-angle and in some cases density. Sheath potentials at antenna limiters are computed and compared to experimental observations from AUG and WEST, supplemented by poloidal profile analyses via visible spectroscopy. The implications of curvature effects are also examined during assessments of a flat model of the AUG three-strap antenna (Petra-M) and a curved model of the WEST antenna (COMSOL).

* Corresponding author: guillaume.urbanczyk@cnrs.fr

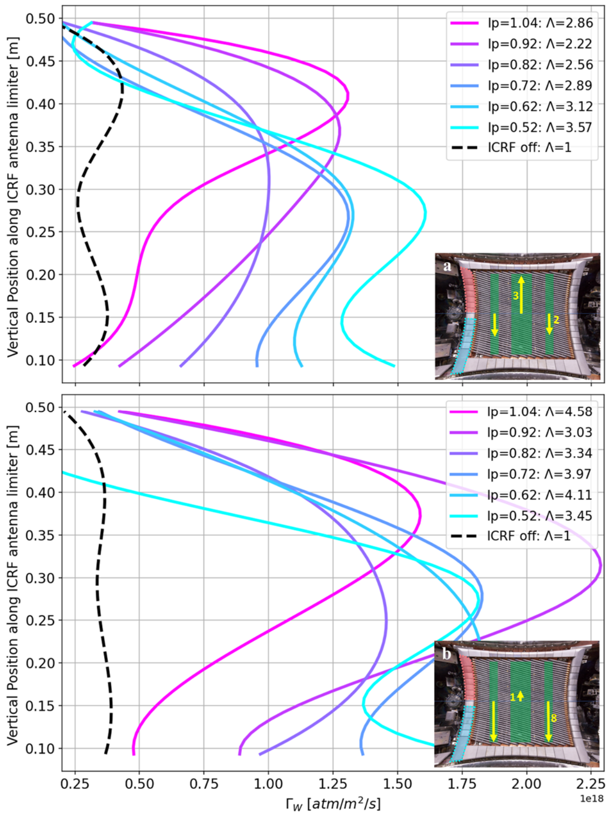

Figure 1. W outflux (gross erosion) **measured** along AUG antenna limiter **with visible spectroscopy** for various plasma currents (Ip [MA]), dipole phasing (180°), and two different power balances: (top) P_{cent}/P_{out}=3/2 and (bottom) P_{cent}/P_{out}=1/8. For each value of Ip, increase factors Λ were estimated (cf. eq. 1), and the corresponding value of the tilt-angle can be found on the x-axis of Figure 9.

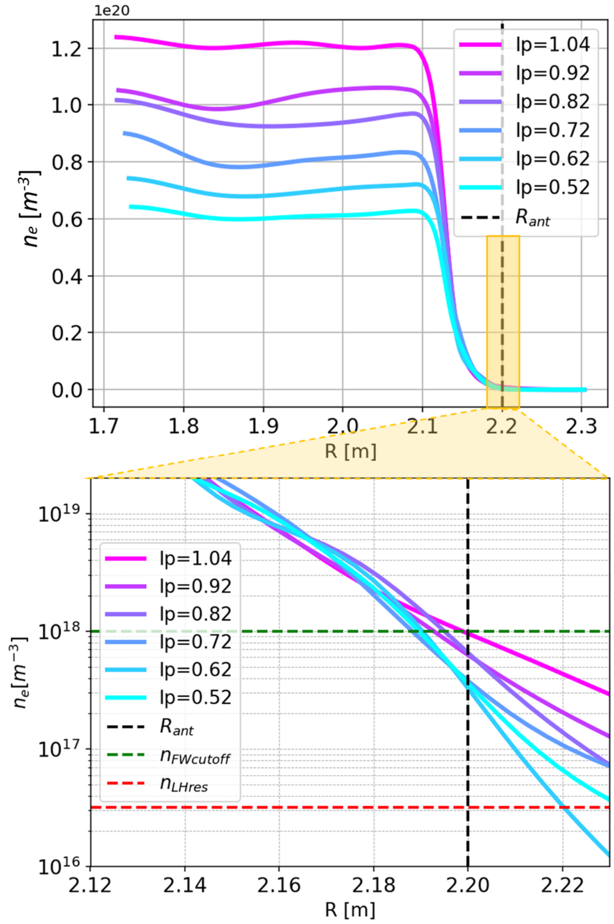

Figure 2. Density profiles from reflectometry in the core (top) and in the edge (bottom) during plasma current (Ip) scan (AUG #37150 cf. Figure 2 in [3] where also error bars are implied)

2 Simulation Methodology

For RF calculation, we model a deuterium plasma with 5% H minority by a cold dielectric tensor with collisions. For erosion calculation, we include small fractions of impurities (0.5% C, 0.5% B, 0.01% W). We systematically compute increase factors, representative of the gross erosion increase, integrated on the whole antenna limiters (eq.1) and Faraday screen (eq.3):

$$\Lambda_{\lim} = \Gamma_{Wtot}^{ICRH \to ON} / \Gamma_{Wtot}^{ICRH \to OFF} \quad (1)$$

with
$$\Gamma_{W\,tot} = \iint_{Limiter} \Gamma_W \quad (2)$$

$$\Lambda_{FS} = \Gamma_{Agtot}^{ICRH \to ON} / \Gamma_{Agtot}^{ICRH \to OFF} \quad (3)$$

with
$$\Gamma_{Agtot} = \iint_{FaradayScreen} \Gamma_{Ag} \quad (4)$$

2.1 Petra-M simulations (AUG flat model)

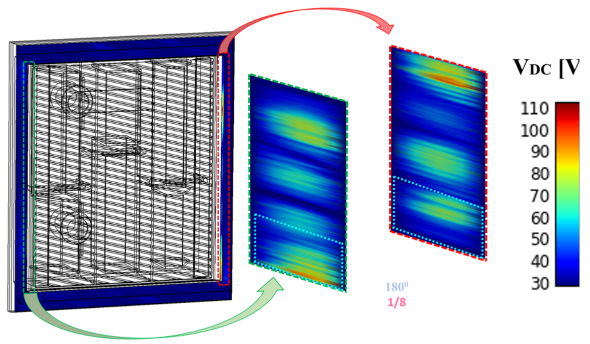

Figure 3. Flat geometry of ASDEX Upgrade 3-strap antenna used in Petra-M simulations, with RF sheath boundary conditions applied on the whole limiter frame, with largest fields appearing only on the inner part of the limiter, hence the focus made on the inner-left surface in Figures 5-6-7 (location best diagnosed).

Petra-M is a FEM multi-physics platform [6]. For this specific work, we employ boundary conditions (BCs) implemented in Petra-M and based on a magnetic potential formulation for both linear and non-linear 3D RF sheath BCs [7, 8] applied only on the limiters. The Faraday Screen typically sits behind the plasma | vacuum interface and is modelled as a Perfect Electric Conductor.

In this study, Petra-M simulations use a simplified flat geometry of the 3-strap ICRF antenna of ASDEX Upgrade (AUG). The simulations explore the influence on rectified potentials (V_{DC}) and tungsten gross erosion (Γ_W) of:

- magnetic tilt-angles: assessed on operational ranges and beyond (fixing the density);
- density modifications induced by the plasma current scan shown in Fig. 2, with a tendency to the higher density at the higher plasma current (in [3] the density profile was fixed at tilt-angle 11° which is the default angle used in most previously published simulations);
- the combination of both effects.

Figures 5-7 show the results of simulations for various parameters. For simplicity, we focus on the region of most interest (the one best diagnosed), which is the inner surface of the left limiter (materialized by green dashed lines in Figure 3). Position x=0 corresponds to the plasma | vacuum interface (in front of the Faraday Screen), and it goes deeper in the plasma as x increases.

2.2 COMSOL simulations (WEST curved model)

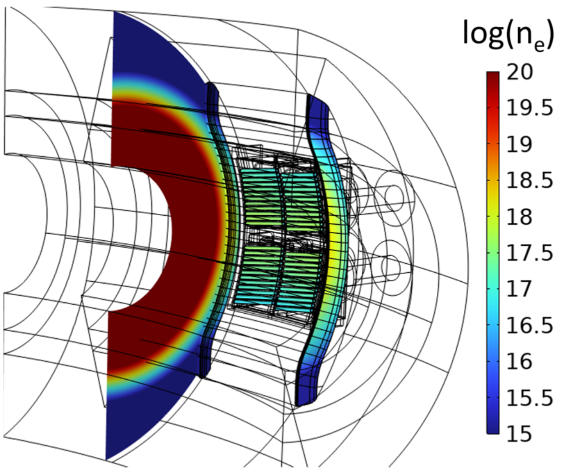

Figure 4. Plasma density on the sheath surfaces of the curved geometry of WEST antenna used in COMSOL simulations, with RF sheath boundary conditions applied not only on the limiters, but also on the Faraday Screen

The COMSOL Multiphysics simulations, employing the sheath-equivalent dielectric layer technique, are used to model the WEST antenna, which features a realistic curved geometry [9]. Unlike the model employed for AUG in Petra-M, COMSOL includes geometric complexities through a finite-element approach, with an artificial sheath layer applied to both the antenna limiters and Faraday Screen bars (Figure 4), with the plasma | vacuum interface just behind as shown in Figure 7 of [9]. This layer mimics sheath effects by incorporating dielectric properties representing sheath impedance. The assumptions specific to COMSOL simulations include a plasma density profile obtained from reflectometry measurements of WEST shot 59789 (cf. Figure 4), and the radial position of the antenna consistent with experimental conditions. In the shadow of antenna limiters, to account for the "private SOL" region, density decays faster (10 cm decay length in addition to the original profile). We acknowledge the decay still is unrealistically slow, but this is the best we can do so far, given numerical limits of mesh thinness required to capture sharp gradients and ensure model convergence. The simulations analyse sheath potentials on both limiters (coated with tungsten) and Faraday Screen (coated with silver) across different magnetic tilt-angles, thereby enabling a comparative evaluation of geometry impacts.

3 Simulations Results

3.1 Petra-M simulations (AUG flat model)

The results from Petra-M simulations for the AUG flat antenna model are summarized as follows. The antenna excitation used in these simulations corresponds to dipole phasing with P_{cent}/P_{out}=1/8 (cf. Fig.1b), unoptimized power balance which excites high electrical field close to the antenna side limiters.

Figure 5 presents the results of the magnetic field tilt-angle scan performed at a fixed density profile (cf. case Ip=0.82 in Figure 1). This figure illustrates the sensitivity of V_{DC} and the associated Γ_W assessed for the realistic plasma mixture shown in Figure 11 of [3], to variations in the magnetic field tilt-angle under the used conditions. We further explore numerically up to a tilt-angle of 22°, beyond the operationally accessible range (limited by maximal plasma current used in the corresponding experiments I_p < 1.2MA → tilt-angle < 14.5°). Values of V_{DC} on average appear lowest when the magnetic field tilt angles is in the range from 14.5° to 17°, i.e. close to the Faraday Screen bar alignment of 15°. Average values of Γ_W mostly follow this trend. Also, the W increase factor – reflecting how much more tungsten is eroded on this part of the limiter when the antenna is powered (cf. equation 1) – is minimal in this range of tilt-angles ($\Lambda = \Lambda_{lim} = 2.5$). Note also that in the calculations, the horizontal striations in Figures 5-7 follow the periodicity of the Faraday Screen bars, an effect usually not observed during experiments where the effect is typically smoothened out.

Figure 6 reveals the influence of the density variation, as observed in the experiment and shown in Figure 2. Here we the tilt-angle is fixed at 11°.

Finally, in Figure 7, the effects of density and magnetic tilt-angle are combined for the experimental range of the tilt-angles. This modifies the amplitude of the variations observed in Figure 5. Neglecting further uncertainties of the density profile measurements, the effect of the magnetic field angle variation is still visible in the calculations: V_{DC}, Γ_W and Λ_{lim} are somewhat lower at 14.5°.

These results hint at the possible effect of alignment of the Faraday screen bars with magnetic field lines on reduction of the near-field induced RF sheath effects and impurity production in fusion devices. One physical explanation is a better screening of the Slow wave ($\boldsymbol{E}_{\parallel}$) when FS bars are parallel to B field lines [10].

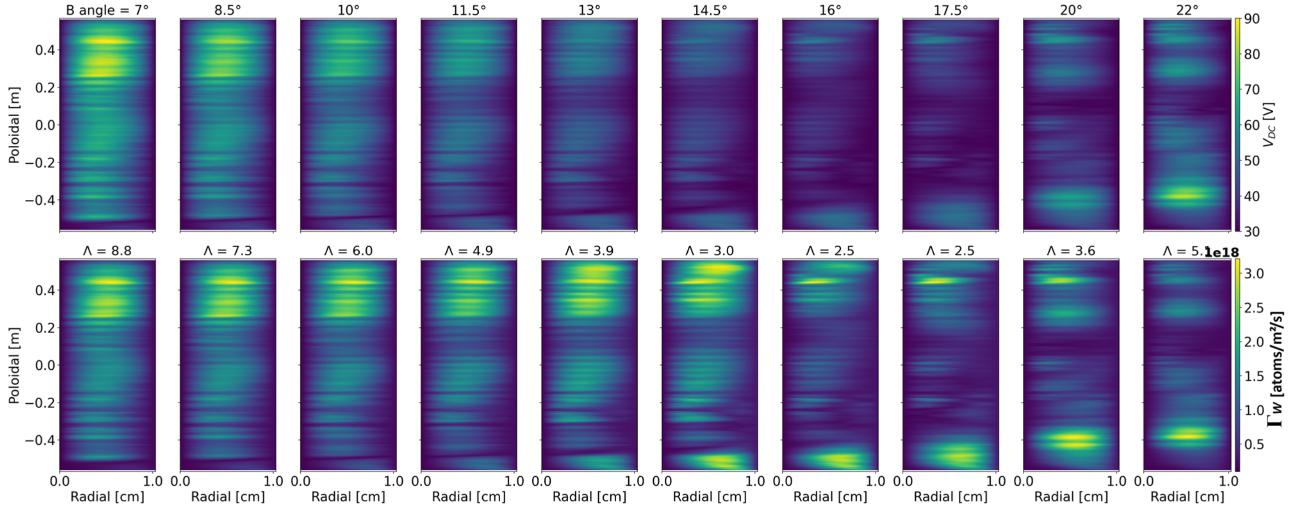

Figure 5. Rectified potential V_{DC} [V] (top row) and tungsten gross erosion Γ_W [atoms/m²/s] (bottom row) on the inner left surface of the AUG 3-strap antenna. B field tilt-angle scan - n_e profile fixed (cf. Ip=0.82 MA in Figure 2).

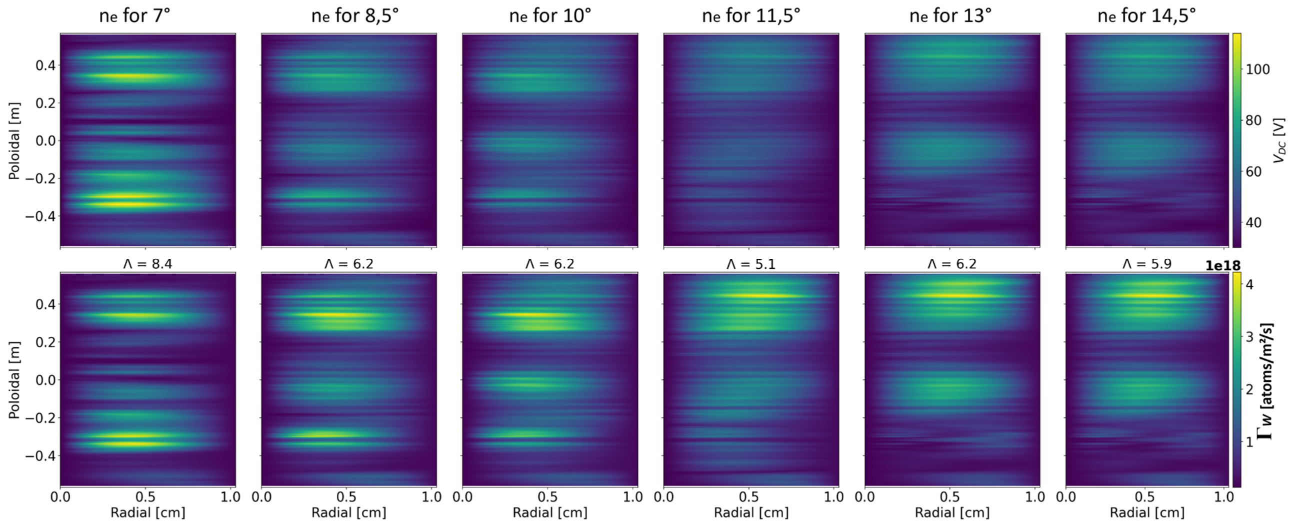

Figure 6. Density scan - B field tilt-angle = 11°.

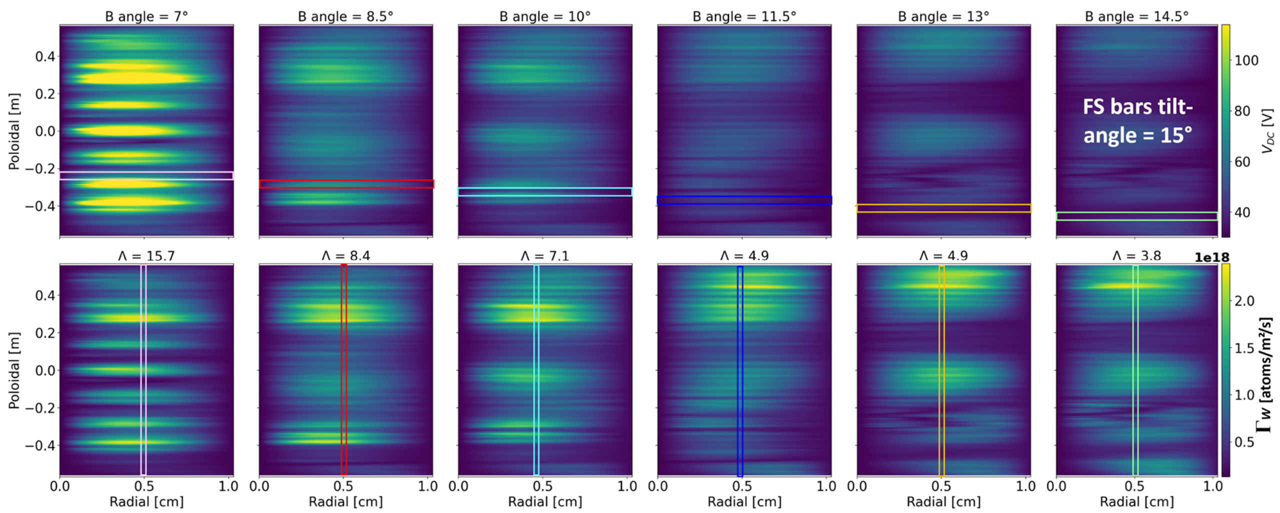

Figure 7. Density and B field tilt-angle scan. Colored rectangles on V_{DC} colormaps represent the area to which the RFA probe magnetically connect in each case, which are the areas combined for synthetically reconstructing the map shown in Figure 10. Colored rectangles on Γ_W colormaps represent the radial location where synthetic profiles shown in Figure 11 are extracted.

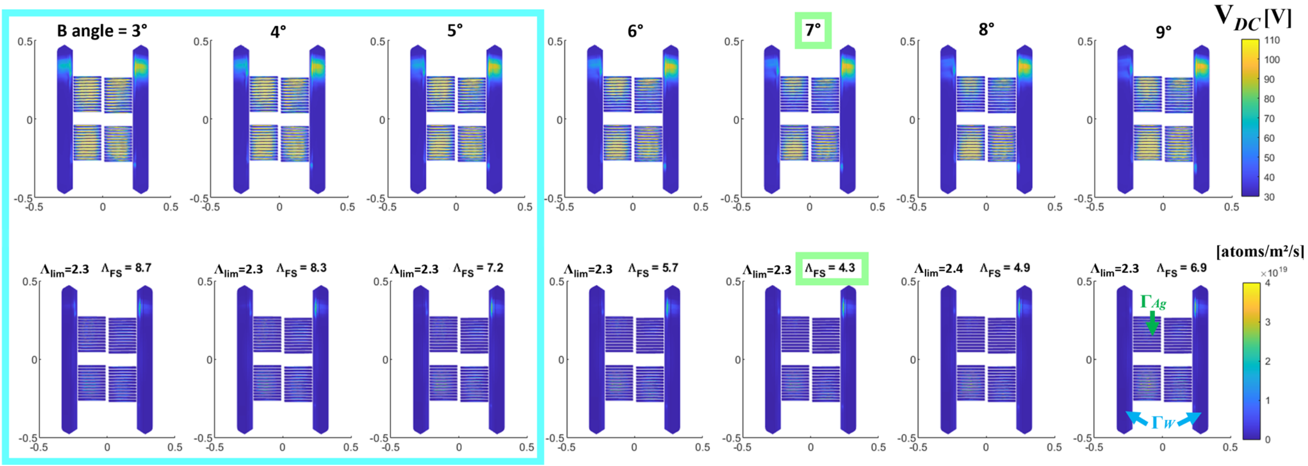

Figure 8. Influence of B field tilt-angle on limiters and Faraday screen. Top row: rectified potential V_{DC} [V]. Bottom row: tungsten gross erosion on limiters Γ_W [atoms/m²/s]; silver gross erosion on Faraday Screen Γ_{Ag} [atoms/m²/s]. Operationally accessible angles materialized by cyan rectangle (300 < I_p < 700 kA).

3.2 COMSOL simulations (WEST curved model)

The COMSOL simulations on the WEST curved antenna model provide further insight into the geometric dependence of RF sheath potentials.

Figure 8 shows for various magnetic tilt-angles, rectified sheath potentials on the antenna front face, W sputtering on the limiters, and Ag sputtering from the Faraday Screen. Unlike observation made with the flat geometry, the results with curved geometry show a very weak sensitivity of rectified potentials on the limiters (Λ_{lim} = 2.3). We are not certain whether the curvature entirely explains this difference, but it the most suspected cause. We plan on confirming this by applying Petra-M code to the same case with the curved AUG geometry, but this is beyond the scope of the present paper.

In contrast, Ag sputtering on the Faraday screen is minimized when the magnetic field lines are aligned on the Faraday Screen bars (7° → cf. green rectangles in Figure 8). In that case, the increase of silver erosion when powering the antenna is minimized (Λ_{FS} = 4.3).

4 Comparisons with experiments

The simulation findings are now discussed in the context of the experimental observations. Figure 9 displays equivalent local RF potentials V_{RF} deduced from the RF currents measured by shunts at various tiles of the AUG antenna limiters. The dependence of V_{RF} as a function of the plasma current shows a similar trend as that obtained for V_{DC} with Petra-M simulations. While red curves correspond exactly to the same antenna excitation as in section 3 (bottom graph in Figure 1), blue curves also show V_{RF} for a well-balanced power on the straps (top graph in Figure 1), showing how good the tapering of the power can mitigate RF fields on the limiter. Thus, the results point out the sensitivity to magnetic field alignment as a possible explanation. However, one has to be careful with this interpretation: in these experiments, the density close to antenna also tends to increase when the plasma current is increased. Although this density dependency serves as an input to the Petra-M calculations presented in Fig. 7, experimental uncertainties of the density distributions and the RF sheath physics which is not included in the code (i.e. the effects beyond those described by the RF sheath boundary condition) can still influence local RF and DC quantities. Also, the full magnetic equilibrium is not accounted for.

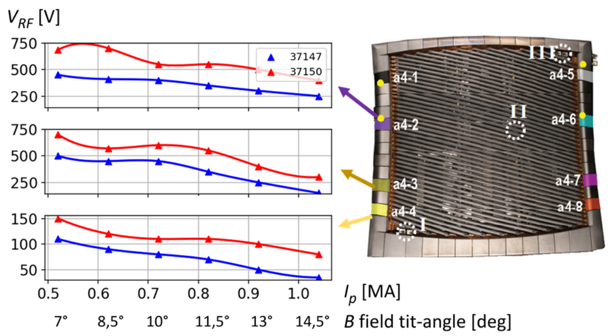

Figure 9. Equivalent RF potentials on various tiles of AUG antenna limiters, deduced from RF current measurements by shunts, as described in [11].

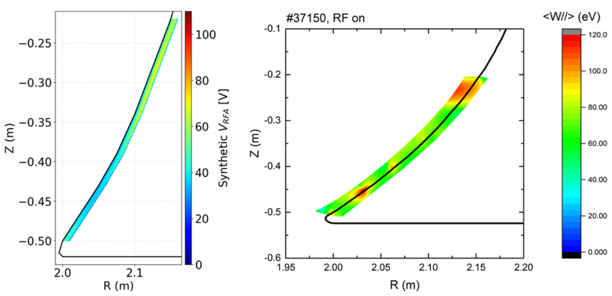

Figure 10. Mean ions energy at limiters. Comparison of synthetic reconstruction from Petra-M calculations (cf. Fig.7a with a map measured near AUG antenna with a reciprocating RFA probe (cf. details in [3]).

Figure 10 shows on the left the 2D map synthetically reconstructed from Petra-M simulations shown on the top row of Figure 7, and on the right, the ion mean energy at the limiters, mapped with the Retarded Field Analyzer (RFA) probe during AUG experiment described in [3].

Map pieces shown by colored rectangles in Fig. 7 are assembled together to reconstruct what the RFA probe should have seen. While broad greenish areas in these maps agree quite well, they differ by several features such as values at the bottom corner and the two red spots registered by RFA. Note that Petra-M sensitivity to the inputs is here of similar order of magnitude as the uncertainties resulting from diagnostics data treatments (density profiles, power coupled, etc.) so that one should not expect perfect agreement. The absence of curvature in the Petra-M model can also partially explain the difference, in particular the smaller potentials at the corner. Yet, large local differences such as the red spots may be the result of mechanisms absent from the model.

Figure 11 shows the result of similar exercise and compares W outflux synthetically reconstructed from Petra-M calculations with profiles measured by visible spectroscopy shown in Fig.1b. Again, the difference between the results, both qualitative and quantitatively (based on increase factors Λ), which relies on a series of assumptions, confirms that what is observed experimentally can differ quite a lot from modelling, and invites us to further think of mechanisms that we neglected, but which may play a crucial role, perhaps such as convective cells.

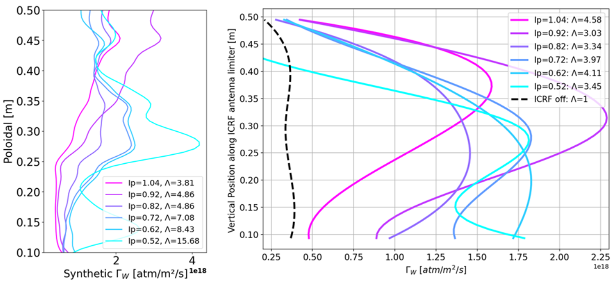

Figure 11. W outflux (gross erosion). Comparison of synthetic reconstruction from Petra-M calculations with profiles measured by visible spectroscopy (cf. Fig.1b).

Figure 12 presents core spectroscopy measurements of Ag^{17+} and Ag^{18+} in WEST discharges at different plasma current, showing clear correlation with the ICRF power. Note first that the presence of Ag is perfectly correlated with the ICRF power; almost no Ag without ICRF. Also, the very similar trend of Ag^{17+} and Ag^{18+} is reassuring regarding an eventual mis-interpretation of these trends; if spectral lines were somehow "polluted" by other species emitting at similar wavelength. Ag content also seems to increase faster with P_{ICRF} for I_p=400kA than 700kA. Given the quite stable influx of ions on the limiter for both discharges (cf. DI on the 3rd panel), these data support a correlation between magnetic tilt-angle alignment and reduced core Ag content, in a good agreement with COMSOL predictions. Interpretation can yet be more complex considering different edge densities registered.

Results of a full I_p scan experiment in WEST are reported in section 6 of [1] where 2D maps of plasma potentials are measured with a reciprocating emissive probe plunging at different Ip from the top of the machine and magnetically connecting to the top right corner of WEST ICRF antenna, nearby maximal V_{DC} predicted by simulations in Fig. 8.

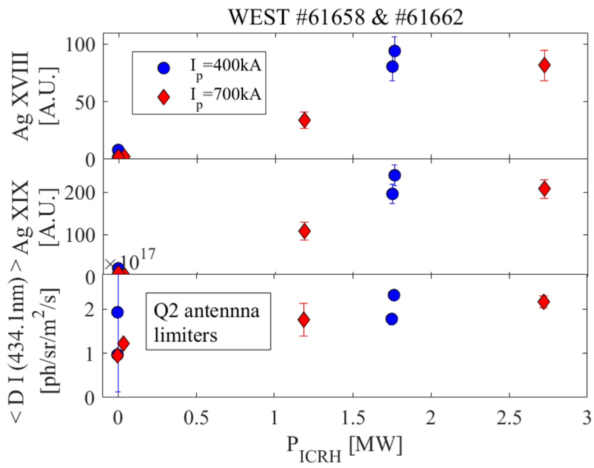

Figure 12. Brightness of two lines of Ag measured in the core of WEST by UV spectroscopy, versus total ICRH power, for pulses at Ip=400kA (#61662, magnetic tilt angle ~ 3°) and for Ip=700kA (#61658, tilt angle ~ 5°). D I line brightness averaged over antenna side limiters in the same time windows.

Note that V_{DC} insensitivity to the tilt angle observed in Figure 8 suggest that measurements in [1] are à priori fully representative of V_{DC} spatial variation. In addition, to try compensating for the density influence on wave coupling efficiency, voltages on coaxial lines and Greenwald fraction were kept constant during the experiment. Regarding Ag content in the core, since the experiment was made shortly after boronization, the dominant effect observed is unfortunately the shot-to-shot erosion of the boron layer on the FS screen, rather than the effect of the B field tilt angle.

5 Conclusion

This study has investigated how ICRF-induced near-field effects depend on magnetic field geometry by the means of analysis of numerical simulations and comparisons with experimental diagnostics in AUG and WEST tokamaks. Using Petra-M simulations for the AUG flat antenna model and COMSOL simulations for the curved WEST antenna, we find **indications that aligning the B field lines with the Faraday screen bars can indeed help reducing sheath rectification and associated impurity sputtering.** This analysis, however, is hampered by various effects imposed by density variations in the experiments.

On the ***limiters*** of the AUG flat model, potentials show a sensitivity to the alignment, whereas no such sensitivity is observed on the WEST curved limiter. We suppose this can be due to the curvature, but this still needs to be confirmed. On the ***Faraday screen***, trends on the WEST antenna with Ag eroded during experiments encourage to align the magnetic field lines with the Faraday screen bars.

Further **comparisons with experiments** — including RF potential measurements with shunts, RFA-mapped ion energies and gross erosion measured by visible spectroscopy — partially support these findings. Besides, differences in particular on synthetically assessed gross erosion suggest that we may have neglected key mechanisms in our model.

Beyond antenna front face design, the magnetic alignment has **broader implications**. Recent experimental evidence [12] suggests that antenna limiters also, when properly aligned with magnetic field lines, may also facilitate the flow of **ExB convective cells** without edge interception (corners). For typical "toroidally aligned" limiters, ExB cells are misaligned with the limiter curvature, therefore convecting hot and dense plasma to some corners, enhancing plasma surface interactions. However, when limiters are "field aligned", the convection occurs along the curvature of the limiter without hitting any corner, resulting in a net reduction of interaction.

All these results together highlight the importance to consider magnetic field alignment in antenna design and component integration to minimize sheath-related effects and improve plasma performance in fusion devices.

7 Acknowledgements

The whole AUG and WEST ICRF teams, are all warmly acknowledged.

This work has been carried out within the framework of the French Federation for Magnetic Fusion Studies (FR-FCM) and within the framework of the EUROfusion Consortium, funded by the European Union via the Euratom Research and Training Programme (Grant Agreement No 101052200 — EUROfusion). Views and opinions expressed are however those of the author(s) only and do not necessarily reflect those of the European Union or the European Commission. Neither the European Union nor the European Commission can be held responsible for them.

This research used resources of the National Energy Research Scientific Computing Center (NERSC), a U.S. Department of Energy Office of Science User Facility located at Lawrence Berkeley National Laboratory, operated under Contract No. DE-AC02-05CH11231. The PPPL work was supported by the US Department of Energy under Contract Number DE-AC02-09CH1146.

References

[1] R. Diab et al., Direct Measurement of ICRF-Enhanced Plasma Potentials Using Reciprocating Emissive Probes on the WEST tokamak, 25th Topical Conference on Radio-Frequency Power in Plasmas, Schloss Hohenkammer, Germany, May 19-22 (2025).

[2] M. Kubic et al., Measurement of sheath potential in RF-biased flux tubes using a retarding field analyzer in Tore Supra tokamak, J. Nucl. Mater. **438**, S509–12 (2013), https://doi.org/10.1016/j.jnucmat.2013.01.105

[3] G. Urbanczyk et al., Characterization of W production during ICRF operations: experiments and modeling, Nucl. Fusion **65**, 046018 (2025). https://doi.org/10.1088/1741-4326/adbd52

[4] L. Colas et al., Localized Scrape-Off Layer density modifications by Ion Cyclotron near fields in JET and ASDEX Upgrade L-mode plasmas, J. Nucl. Mater. **463**, 735–738 (2015). https://doi.org/10.1016/j.jnucmat.2014.10.011

[5] V. Bobkov et al., Impact of ICRF on the scrape-off layer and on plasma wall interactions: From present experiments to fusion reactor, Nuclear Materials and Energy **18**, 131–140 (2019). https://doi.org/10.1016/j.nme.2018.11.017

[6] S. Shiraiwa, et al., RF wave simulation for cold edge plasmas using the MFEM library, EPJ Web of Conferences **157**, 03048 (2017). https://doi.org/10.1051/epjconf/201715703048

[7] S. Shiraiwa et al., Magnetic potential based formulation for linear and non-linear 3D RF sheath simulation, Nucl. Fusion **63**, 026024 (2023), https://doi.org/10.1088/1741-4326/aca6f9

[8] S. Shiraiwa et al. Finite element modeling of RF waves in fusion plasmas: progress in past decades and future role, 25th Topical Conference on Radio-Frequency Power in Plasmas, Schloss Hohenkammer, Germany, May 19-22 (2025). https://www.ipp.mpg.de/5487515/Talks

[9] W. Tierens et al., Radiofrequency sheath rectification on WEST: application of the sheath-equivalent dielectric layer technique in tokamak geometry, Nucl. Fusion **64**, 126039 (2024). https://doi.org/10.1088/1741-4326/ad80a9

[10] M.L. Garrett and S.J. Wukitch, Mitigation of radio frequency sheaths through magnetic field-aligned ICRF antenna design, Fusion Engineering and Design **87**, 1570–1575 (2012). https://doi.org/10.1016/j.fusengdes.2012.04.011

[11] V. Bobkov et al., Making ICRF power compatible with a high-Z wall in ASDEX Upgrade, Plasma Physics and Controlled Fusion **59**, 014022 (2017). https://doi.org/10.1088/0741-3335/59/1/014022

[12] R. Diab et al., Mitigation of ICRF—edge plasma interaction in Alcator C-Mod, Nucl. Fusion **65**, 076038 (2025). https://doi.org/10.1088/1741-4326/ade456